Nuclear Materials and Energy 45 (2025) 102003

Contents lists available at ScienceDirect

Nuclear Materials and Energy

journal homepage: www.elsevier.com/locate/nme

Erosion of thin boron films at the linear plasma device PSI-2 during deuterium discharges: Atomic and molecular spectroscopy of boron ☆

Marc Sackers [a,*], Oleksandr Marchuk [a], Anne Houben [a], Eduard Warkentin [a], Marcin Rasinski [a], Sebastijan Brezinsek [a,b], Arkadi Kreter [a]

[a] Forschungszentrum Jülich GmbH, Institute of Fusion Energy & Nuclear Waste Management - Plasma Physics, 52425, Jülich, Germany
[b] Heinrich Heine University Düsseldorf, Faculty of Mathematics and Natural Sciences, 40225, Düsseldorf, Germany

ARTICLE INFO

Keywords:
Boron
Erosion
Fusion
Spectroscopy
Low-temperature plasma

ABSTRACT

This study reports on deuterium plasma-boron layer interaction investigated at the linear plasma device PSI-2. In preparation, RF magnetron sputtering deposited 115 nm thick boron layers onto tungsten substrates. Exposing the samples to a deuterium plasma in PSI-2 provided the bombardment by ions. The discharge conditions in PSI-2 were chosen such that the bombardment was predominantly due to deuterons (D^+) impinging at normal incidence. This operating scenario yielded a typical ion flux density onto the sample of 4×10^{21} m^{-2} s^{-1}. Varying the bias applied to the sample from −43 V (floating potential) to −100 V allowed for investigating the near-threshold erosion regime.

The B I 2p-3s transition (249.7 nm), and the BD A-X transition (432.8 nm) provided the time-resolved (10 s) spectroscopic fingerprint of physical and chemical erosion during the plasma discharges of 70 s duration. The emission of the BD molecular band depends only weakly on the bias applied to the sample. Notably, this emission is also present at the lowest impact energies, suggesting a contribution by chemical erosion. Contrary to that, atomic boron emission follows reasonably close to the expectations by the binary collision approximation (BCA). The post-mortem layer thickness characterization reveals net sputtering yields that exceed the predictions by BCA and agree well with data from Hechtl et al. (1992).

1. Introduction

The ITER Organization proposed a new baseline that primarily focuses on reevaluating the wall material [1,2]. Tungsten is now considered the first-wall material, as opposed to the previously selected beryllium. A key weakness of beryllium is the much lower melting point (1290 °C) compared to tungsten (3400 °C), so that fast transient events are potentially more destructive in the case of a Be first-wall. In addition, the physical sputtering by fuel particles (D, T) is orders of magnitude smaller for tungsten [3], significantly prolonging the lifetime of the wall material. This re-baseline comes at the cost of losing the strong oxygen gettering capabilities of beryllium.

Minimizing oxygen concentration in fusion plasmas through the gettering process has immensely enhanced discharge stability [4]. One way to reduce the oxygen concentration is to introduce additional chemistry by conditioning the reactor wall. A highly successful method addressing this challenge is the boronization of the reactor wall. It was initially developed for the TEXTOR tokamak [5] and has since seen a lot of application in other fusion experiments [6–10]. For example, Fig. 3 of [6] (ASDEX) and Fig. 4 of [8] (W7-X) illustrate the influence of boronization on the oxygen concentration via emission spectroscopy. The contribution of impurities to the spectra measured dropped notably due to wall conditioning via boronization. At the same time, this impurity control – mainly the reduction in oxygen concentration – significantly reduces the sputtering of high-Z elements such as tungsten.

However, any notable changes in the elemental composition of the reactor wall at ITER modify the plasma-wall interaction (PWI). These changes can drastically influence the erosion behavior of the plasma-facing components and the migration of this material into receded areas. One code simulating the PWI for ITER, and gives information about W sources and W screening, is the kinetic Monte Carlo code ERO2.0 [12–14]. As another example, it predicts the deposition of sputtered material onto the first mirrors of optical systems in ITER [15,16]. Retaining high specular reflectance of the mirrors is essential for ensuring acceptable working conditions for diagnostics, such as the core charge exchange recombination spectroscopy system [17] or the core Thomson scattering diagnostic [18]. As it turns out, boron causes

☆ This article is part of a Special issue entitled: 'PFMC-20' published in Nuclear Materials and Energy.

* Corresponding author.
E-mail address: m.sackers@fz-juelich.de (M. Sackers).

https://doi.org/10.1016/j.nme.2025.102003
Received 14 July 2025; Received in revised form 26 September 2025; Accepted 13 October 2025
Available online 15 October 2025

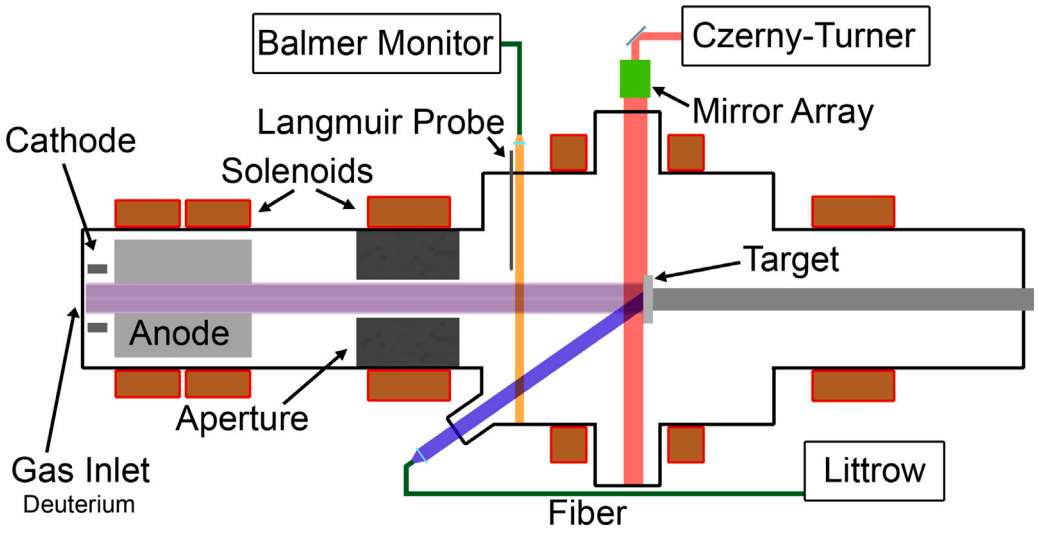

Fig. 1. Schematic of the optical emission spectroscopy setup used at the linear plasma device PSI-2 during plasma-boron layer interaction in deuterium discharges. The Balmer Monitor is a 4-Channel Avantes USB spectrometer providing information on the plasma stability. The Czerny-Turner spectrometer (Fig. 3.6 of [11]) measures the resonant 2p-3s transition of boron, and the Littrow spectrometers (Fig. 3.4 of [11]) detect the resonant BD AX Q-branch. Sections 3 and 4 motivate the choice of the optical transitions studied in this work.

unfavorable deposition on such diagnostics since even thin films can drastically degrade the optical properties of the first mirrors [19].

Currently, there are still significant uncertainties regarding the physical and chemical erosion rates of the boron layer [20]. Experimental data measured by [21] give sputtering yields that significantly exceed the predictions by the binary collision approximation in the near-threshold regime of physical sputtering [3]. The source of the boron erosion, in essence, physical or chemical erosion, has a massive implication for the migration of boron within a fusion reactor: Typical energies of sputtered particles are on the order of the surface binding energy - a few eV [3]. Chemically released species often carry energies reflecting the thermal energy of the surface, which is well below 1 eV (11 604 K) [22]. This mismatch in kinetic energy provides different ionization lengths, and plasma chemical processes, such as dissociation, must be considered for molecules [23]. Another challenge is the need for validated collisional data of the molecules (cf. data for CH_y in [24]). Thus, further experimental data is needed to investigate the near-threshold erosion of boron by deuterium bombardment.

This work reports on plasma-boron layer interaction studies performed at the linear plasma device PSI-2. A 115 nm thick boron layer, deposited by magnetron sputtering, covering a polished tungsten substrate, was subjected to particle irradiation. Pure deuterium discharges at PSI-2 provided the deuterons to bombard the boron layer. Varying the bias applied to the sample allowed us to investigate the near-threshold regime of the physical sputtering. The plasma-boron layer interaction releases atomic boron and boron deuteride. Specifically, the BD molecule is assumed to be produced via chemical erosion, and its emission provides the spectroscopic fingerprint for this erosion process. So, time-resolved atomic and molecular spectroscopy enables the qualitative evaluation of the physical and chemical erosion, respectively.

This paper is structured in the following way: Section 2 introduces the experimental setup and provides information on the plasma parameters. It also discusses the plasma scenario chosen. Sections 3 and 4 deal with selecting adequate optical transitions for measuring the emission by the atomic and molecular species. Moreover, it outlines the steps taken for the spectral calibration and validates the molecular modeling by using the BH molecule as a proxy for BD. Section 5 reports on the erosion experiments and describes the information contained within the atomic and molecular spectra. The erosion rates at different impact energies of the deuterons are given in Section 6. Finally, Section 7 concludes the paper and Section 8 provides a brief outlook.

2. Experimental setup

Fig. 1 presents a sketch of the linear plasma device PSI-2 [25]. It is based on an arc discharge, ignited between a hollow-ring-shaped cathode and anode. Six solenoids create the axial magnetic field, shaping the plasma into the characteristic linear column. This plasma terminates at the target plate, providing the plasma-wall interaction.

A radially movable Langmuir probe provides the current voltage characteristic for estimating plasma parameters, as Figs. 2(a) and (b) illustrate. In this study, the electron temperature peaks at 10 eV, and the highest electron density is 3×10^{17} m^{-3}. The geometry of this source creates a hollow plasma profile. That is the ion flux density peaks for standard deuterium discharges at a radius of 2.2 cm. In this case, the cathode current is 100 A, and the D_2 gas flux into the source is 100 sccm. A differential pumping stage allows for the decoupling of the ions from the neutral particles. So, the pressure within the region dedicated for plasma-wall interaction studies was, in this case, 0.014 Pa. A critical parameter is the ionic species that bombard the plasma-contacting surface. Therefore, choosing the discharge conditions known for the lowest D_2^+ and D_3^+ concentrations in PSI-2 ensured the erosion of the plasma-contacting surface primarily due to deuterons (D^+). This choice requires setting the power of the arc discharge to 6.7 kW (cf. Tab. 1 of [26]).

Additionally, impurities, monitored by a quadrupole mass spectrometer, may also provide significant erosion of the boron layers. The main impurity in deuterium discharges in PSI-2 is oxygen with a concentration below 0.3% – see discussion in Section 4.1.1 of [27]. So the erosion of the low-Z boron layer by the mid- and high-Z impurities is insignificant.

The kinetic energy of the bombarding deuterons results from the difference between the plasma potential and the potential applied to the sample holder. The plasma potential developing in PSI-2 depends on the difference in cross-field transport of electrons and ions: The Larmor radius of the electrons at the 90 mT magnetic field of PSI-2 is much smaller than the diameter of the plasma column, resulting in strongly magnetized electrons. Contrary to that, typical ions within PSI-2 (noble gases, H, D, etc.) have a larger gyro radius, which can be in the order of the 6 cm plasma diameter. The imbalance in cross-field transport of electrons and ions is compensated by a negative plasma potential that develops in the center. This behavior is apparent in Fig. 2(b): the kinetic energy of the ions that bombard the sample holder has

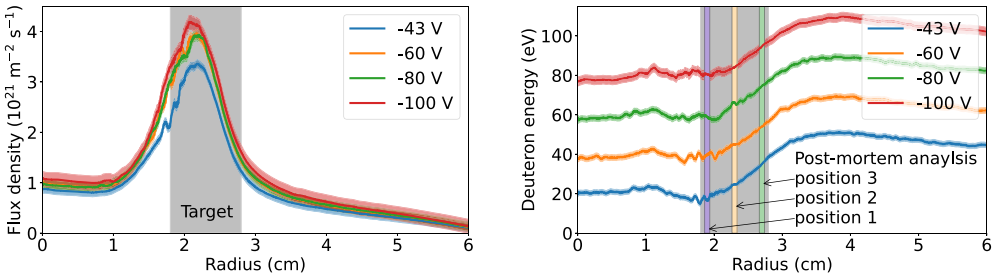

(a) Flux density of the deuterons

(b) Kinetic energy of the deuterons impacting on the sample holder

Fig. 2. The radially movable Langmuir probe (cf. Fig. 1) provides the sharply peaked plasma profile. During D plasmas, the electron density peaks at approximately 3×10^{17} m^{-3}, and the highest electron temperature is on the order of 10 eV. The curves in both figures show the data points smoothed by a Savitzky-Golay filter, and the areas shaded in the same color as the curve represent the standard deviation. (a) shows the ion flux density of the discharge scenarios used during plasma-boron layer interaction studies. (b) presents the kinetic energy the ions gain due to the potential drop between the plasma and the biased sample holder.

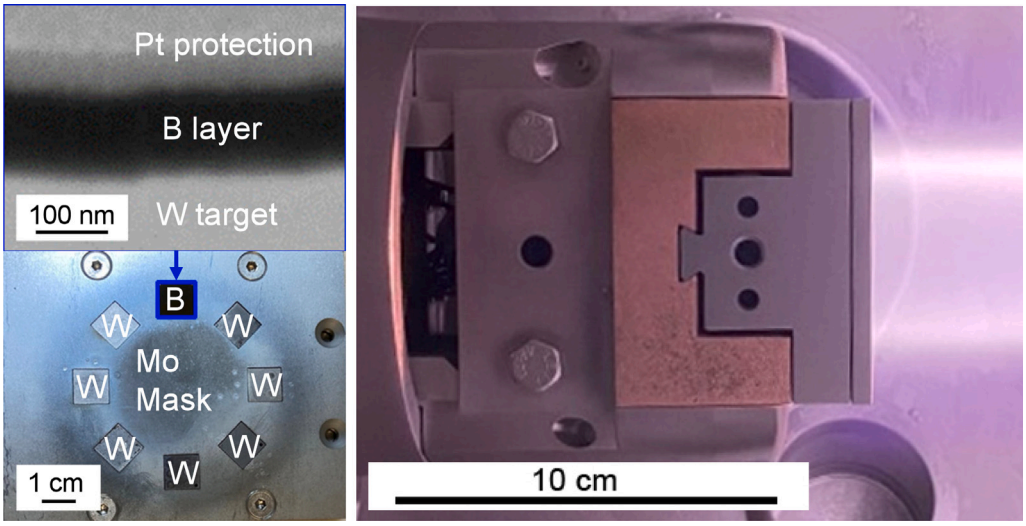

(a) Boron layer thickness and sampler holder

(b) Side-view into the linear plasma device during a deuterium discharge

Fig. 3. (a) shows the boron layer thickness characterization before plasma exposure, using FIB cutting followed by SEM at an angle of 54°. These samples are mounted into the sample holder. In this case, we erode the boron layer, while the kinetic energy of D^+ (<100 eV) is insufficient for sputtering the Mo mask and the seven W catcher samples.

a pronounced gradient in the radial direction. The post-mortem analysis at positions 1–3 provides the local erosion rates following the plasma exposure experiments, as reported in Section 6.

The choice of discharge condition based on [26] limits the minimal amount of kinetic energy the deuterons can gain. Specifically, the ion and electron currents on a floating target plate are inherently self-compensating, resulting in a stable global floating potential in the absence of an applied bias. It turns out that using the standard deuterium discharge conditions at PSI-2 produces a floating potential of −43 V at the sample. Additional biasing of the target plate at PSI-2 can only lower the potential, increasing the overall drop in potential to the plasma.

2.1. Preparation and mounting of boron samples for plasma exposure

Fig. 3(a) depicts the thickness of the boron layer deposited via magnetron sputtering onto a tungsten substrate. Houben et al. [28] present more details on the production of these thin boron layers and their characterization. The cross-section of the sample presented stems from scanning electron microscopy (SEM) across a focused ion beam (FIB) cut into the sample. The thin Pt layer on top serves solely to protect the B layer during the FIB cutting process. Fig. 3(a) shows that the boron layer and tungsten target can be clearly distinguished, making it similar to the FIB line marking used in [29]. Thus, retaining a complete, albeit partially eroded, boron layer enables local measurements of the erosion rate at the positions indicated in Fig. 2(b). The thickness of the boron layer amounts to approximately 115 nm. This boron sample (1 cm × 1 cm) is mounted in the top location of the water-cooled sample holder, which is capable of holding eight samples. The remaining seven samples consist of tungsten and act as catcher samples. Estimates using the binary collision approximation show that the 100 eV deuterons are below the physical sputtering threshold of Mo and W [3,30]. This ensures that erosion of the boron layer is dominant. Setting 100 eV as the maximal kinetic energy of the deuterons is also reasonable from a physics point of view since the near-threshold erosion regime of boron is of particular interest: the role of chemical and physical erosion requires further investigation.

Table 1
Spectrometers used during this experimental campaign. The full width at half maximum obtained by line emission from metals gives the line width ($\Delta\lambda$). The resolving power is $\lambda/\Delta\lambda$.

Spectrometer	Avantes[a]	Czerny-Turner	Overview Littrow	High-resolution Littrow
Task	Plasma stability	Physical erosion	Chemical erosion	Chemical erosion
Transitions	D_α ... D_δ	B I 249.7 nm	BD 432.8 nm	BD 432.8 nm
Grating	Ruled	Holographic	Ruled	Ruled (Echelle)
Lines/millimeter	1800	1200	1200	78
Spectral order	1	1	2[b]	56[c]
Spectral range	298–890 nm[a]	236–263 nm	431–437 nm	432.54–433.22 nm
Line width (nm)	0.16	0.05	0.03	0.004
Resolving power	3 000	5 000	14 000	110 000

[a] Type: AVS-DESKTOP-USB2, 4 channels (CH). CH1: 298–456 nm; CH2: 545–584 nm; CH3: 583–685 nm; CH4: 684–886 nm.
[b] 1. order is also possible but comes at the cost of worse spectral resolution.
[c] At the wavelength of 432.8 nm.

2.2. Spectroscopy setup

All spectrometers, indicated in Fig. 1, fulfill vital roles in the boron erosion experiments. Table 1 presents an overview of the spectrometers' specifications, while the following discussion describes their contribution to the experiments.

The Balmer monitor is a 4-channel spectrometer (Avantes) that measures the visible deuterium Balmer series (D_α... D_δ) at the same cross-sectional plane as the Langmuir probe.

The resonant B I 2p-3s doublet at 249.7 nm is the line chosen for measuring the emission by atomic boron — see Czerny-Turner in Table 1. However, measuring in the UV spectral range can introduce additional challenges, such as low transmission through lenses/windows (Fig. 3.9 of [31]), low reflectance of mirrors (Fig. 3.14 of [31]), and a significant change in the effective focal length [32].

The spectrometers in the Littrow configuration, hereinafter Littrow's, measure the BD A-X band emission (transition) in the visible spectral range.

3. Atomic boron lines and calibration

Boron's electronic groundstate configuration is the $1s^2 2s^2 2p$ doublet, and the next configuration lies within the core-excited quartet of $1s^2 2s 2p^2$ at approximately 3.5 eV. This difference in energy corresponds to a transition occurring at a wavelength of 350 nm. However, it is an extremely weak spin-changing (intercombination) line since relativistic effects are still exceedingly small in boron. So, the line selection for atomic boron requires additional discussion.

The electronic structure of boron guarantees that the sputtered atoms are only within the ground state before entering the plasma, whereas other levels obtain population via electron impact excitation. The transition probability serves as the primary selection criterion for the B I lines: Strong electric dipole transitions of neutral atoms within the visible range have transition probabilities of around $1 \times 10^8\ s^{-1}$ (cf. Eq. (3.57) of [33]). The actual cutoff chosen is $1 \times 10^5\ s^{-1}$ to get better insights into all possible transitions, especially in the visible range. The second selection criterion is a high electron impact excitation rate coefficient ($\langle\sigma\mathbf{v}\rangle$) that depends, of course, on the electron temperature. Section 2 presented typical plasma parameters of the standard deuterium discharge in PSI-2, where the peak electron temperature is 10 eV. Thus, we only consider atomic states below 10 eV. The angular momentum ($\tilde{J}$) resolved Grotrian diagram in Fig. 4 visualizes the dipole transitions that meet the requirements.

The transitions highlighted by the bold and colored lines have sizeable transition probabilities ($>1 \times 10^7\ s^{-1}$) within the doublet system of boron. Photon emission coefficients [$cm^{-3}s^{-1}$] tabulated in the ADAS [35] database (file *ionelec_pec#b0.dat*), which are calculated by solving the stationary rate equations ($\frac{dN_i}{dt} = 0$) for electron impact excitation, confirm that these should be intense lines at PSI-2. The green lines are the 2p-3s transitions. These lines benefit from abundant experimental and theoretical data on isotope and hyperfine splitting [36–38]. However, they can suffer from line blending. The alternative is the strong 3s-3p transition, occuring at a wavelength of 1166 nm (violet-colored lines) [39].

In this study, the major constraint was the camera installed in the available Czerny-Turner spectrometer. Its pixels are silicon photodiodes, whose bandgap is 1.12 eV [40]. The energy of a 1166 nm photon (1 eV) is insufficient to overcome this gap, making it impossible for the camera to measure the IR line. Consequently, the choice is the 2p-3s transition, which is a doublet in the UV region around 249.7 nm.

The 2p-3s transitions have one striking advantage compared to the 3s-3p (1166 nm) lines. The intensity ratio of the 2p-3s lines, omitting self-absorption, is well defined by the branching ratio. That is, the transition into the lower level with $\tilde{J}$=3/2 is twice as strong as the one into $\tilde{J}$=1/2. This behavior is simply a result of the degeneracy ($2\tilde{J}$+1).

Calibrating the Czerny-Turner spectrometer follows the same recipe shown in [41]. In this case, the spectroscopic fingerprint of Si and B hollow cathode lamps (HCLs) provided the data need for deriving the reciprocal linear dispersion. The spectral range covered is 27 nm, and the spectral resolution ($\lambda/\Delta\lambda$) greater than 2500 is sufficient to separate the two B I 2p-3s lines ($\Delta\lambda$ =100 pm).

4. BD transitions and calibration

Selecting the transition of the BD molecule is more straightforward, as Table 1 of [42] indicates: An electric dipole-allowed transition into the ground state ($X^1\Sigma$) originates from the first excited level within the singlet states ($A^1\Pi$). The energy separation (T_0) of $A^1\Pi$ to the ground state is 2.9 eV. Therefore, one expects a large rate coefficient due to electron impact excitation in the T_e =10 eV deuterium plasma at PSI-2. Many fields investigating BH or BD spectra rely on this transition as a fundamental reference point [43–46].

The calibration procedure for the Littrows to measure the BD emission spectra is analogous to that of the Czerny-Turner spectrometer, as described in Section 3. The Mo and V HCLs (typical electron temperature below 1 eV [47]) provide excellent wavelength calibration data in the spectral region around 433 nm. In addition, the B HCL used contains small amount of hydrogen. Thus, the $A^1\Pi$ to $X^1\Sigma$ transition of BH could be measured. Such spectra allow for benchmarking the modeling code of the rotational band spectrum.

The molecular constants of BH and BD, tabulated in Tables III and IV of [48], are used for the modeling. Plugging the constants into Eq. (1) of [48] provides the energy shift of the $A^1\Pi$ and $X^1\Sigma$ molecular levels, depending on the rotational quantum number J and vibrational quantum number v.

The electronic transitions of the BH $A^1\Pi\ |J,\ v\ >$ to $X^1\Sigma\ |J',\ v'\ >$ system have a vanishingly small probability for $\Delta v \neq 0$, as the Franck–Condon factors shown in Table X of [49] indicate. Therefore,

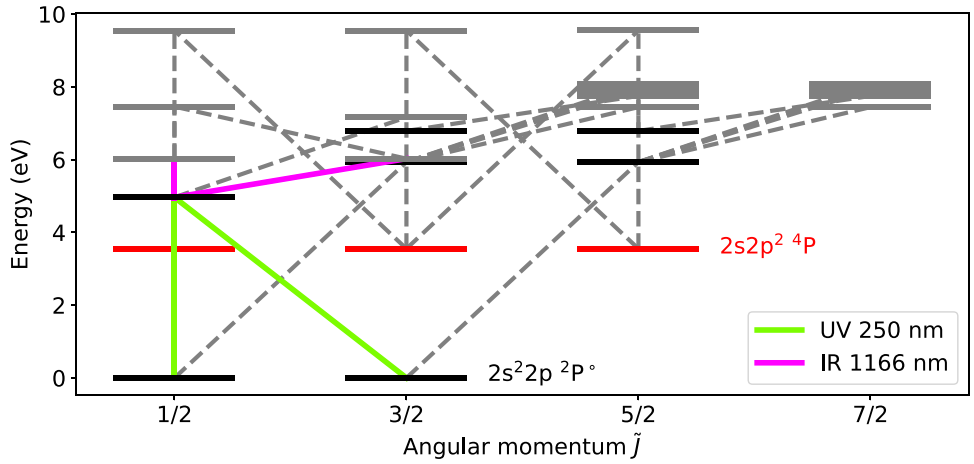

Fig. 4. Reduced Grotrian diagram based on NIST data [34]. We show only observed lines within the spectral range of 200 nm to 1300 nm whose transition probability exceeds $1 \times 10^5\ s^{-1}$. The strong resonant lines with the longest wavelength (249.7 nm) originate from the 2p-3s transition. In our work, we measure this transition.

the spectra measured and modeled are only the rotational band spectra. That is, the selection rules for the quantum numbers are $\Delta v = 0$ and $\Delta J = +1, 0, -1$, known as the R-, Q-, and P-branch, respectively (cf. Chapter IV Section 4 (b) of [50]). In the following, the notation is compressed by referring to the $A^1\Pi\ |v\rangle$ to $X^1\Sigma\ |v\rangle$ rotational band spectra as A-X (v, v).

The rotation of the diatomic molecules also influences the line strength of the transition. Therefore, we use the Hönl-London factors from Eq. (IV, 82) of [50]. The final element needed is the population distribution across the rotational levels, which typically is a Boltzmann distribution

$$N_J \propto (2J+1)\exp\left(-\frac{E_J}{k_B T_{rot}}\right), \tag{1}$$

where E_J is the energy eigenvalue of the rotational level, k_B is the Boltzmann constant, and T_{rot} is the rotational temperature. As a first step, we compared the output of the procedure described above to the results of the PGOPHER [51] code when feeding the molecular constants [48] into it and by assuming a rotational temperature of 2000 K. Both approaches yield identical line positions and intensities, validating the approach.

Figs. 5(a) and (b) present the rotational band spectra of the A-X transition measured using the boron HCL (Ne atmosphere, trace amount of H) at different spectral resolutions. The overview spectrum, recorded with the overview Littrow in first spectral order, has contamination by several Ne II lines. However, the BH Q-branch of A-X (0,0) does not suffer from significant line blending, and the gray shaded area indicates the region where we performed the line fitting. The spectral profile optimized while fitting is a Voigt profile. The fit reproduces the Q-, R-, and P-branches nicely, and the rotational temperature obtained is 557(21) K. Fitting the spectrum of the A-X (1,1) spectrum is a bit more challenging due to the blending with Ne II lines. For instance, the red-shaded direction of the Q-branch indicates a substantial contribution by the Ne II 437.1 nm transition. Thus, the region with line blending was excluded in the fitting the rotational temperature was fixed to the value derived from the A-X (0,0) Q-branch fitting. This fit is in good agreement with the spectrum.

However, the overview Littrow does not resolve the individual transitions within the Q-branch. A higher resolution spectrum would enable the study of possible line blending in a more narrow spectral region. At the same time, the results gain more credibility if the fitting provides essentially the same rotational temperatures at several spectral resolutions. The Littrow with Echelle grating measures at 433 nm in the spectral order 56 and resolves the individual lines of the BH Q-branch, as shown in Fig. 5(b). A narrow bandpass filter with a full width at half maximum of 10 nm suppresses the overlap with other spectral orders. The wavelength calibration reveals that the spectrometer covers a spectral range of 0.67 nm. Fig. 5(b) presents a zoom into the BH A-X (0,0) Q-branch. In this case, one can resolve the individual lines of the branch and distinguish between the two isotopes of boron. Their relative natural abundance matches precisely with the contribution to the spectrum. The rotational temperature amounts to 601(3) K and, thus, differs by less than 7% compared to the one derived using the overview spectrum, validating the spectral analysis.

5. Erosion experiments at PSI-2

The tungsten substrates with approximately 115 nm thick boron layers were exposed to deuteron bombardment at PSI-2. The intensity of the Balmer line series of deuterium provides information on the plasma stability during the pulsed discharges. Fig. 6 presents the temporal evolution of their intensities during a typical discharge length of 70 s. The line intensities increase rapidly during start-up and then decrease to a stable plateau within a few seconds. As such, the plasma parameters stay essentially constant during the erosion experiments.

5.1. Atomic emission during erosion

The Czerny-Turner spectrometer measures the B I 249.7 nm transitions during the erosion experiments. Fig. 7(a) presents the time-resolved intensity detected for a long-pulse case when applying an −80 V bias to the sample. The areas shaded in green indicate phases with plasma operation, during which the B I 249.7 nm doublet (blue, orange) line emission occurs. Taking the ratio of the blue to orange data provides a value fluctuating around 0.5, as shown by the gray line. The plot also includes the red dashed line as a reference to indicate the line ratio expected according to the branching ratio. The gray and red curves agree best during the phases where strong line emission of atomic boron is present. The strongest line emission occurs during the initial plateau phase of about 150 s, indicating a complete coverage of the tungsten surface by a boron layer. Following the plateau phase is a relatively sharp decay of the emission. The transition is not following a step profile. Instead, smoothing of the profile occurs due to the inhomogeneity of the deuteron flux density across the surface (Fig. 2(a)) and the gradient in their kinetic energy (Fig. 2(b)).

Fig. 7(b) presents the line intensities measured during a 70 s pulsed discharge at −100 V bias. Short-pulsed discharges have the advantage of keeping the boron layer from eroding completely off the tungsten sample as the particle fluence is limited. This approach enables the

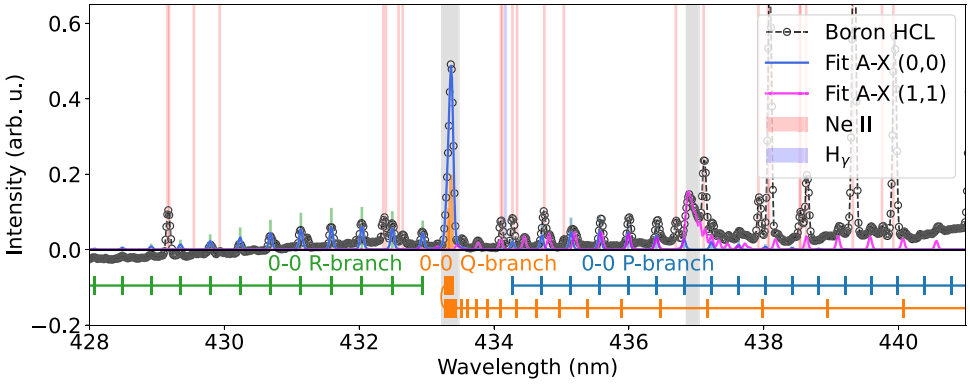

(a) Overview spectrum of the BH A-X (0,0) and (1,1) transitions

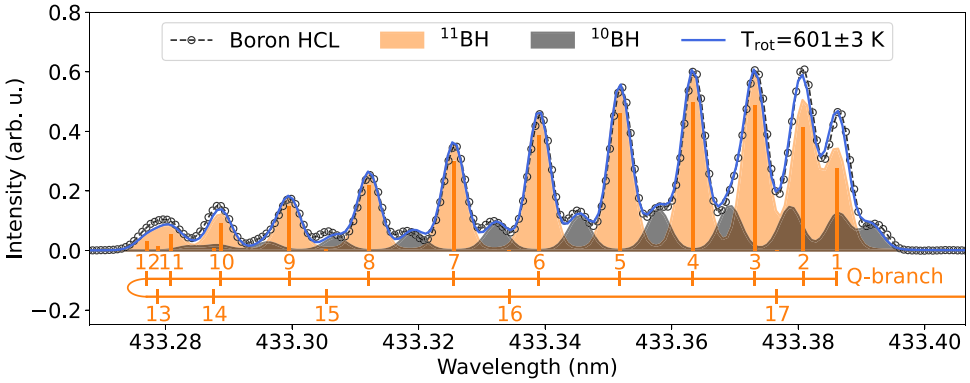

(b) High-resolution BH A-X (0,0) Q-branch spectrum

Fig. 5. (a) Emission spectra of the boron HCL (Ne atmosphere, trace amount of H) around the BH A-X electronic transition. One observes the (0,0) rotational band spectrum clearly and its Q-branch is not polluted by any other spectral line providing a rotational temperature of about 560 K. The (1,1) vibrational transition blends with a few Ne II lines [34]. (b) High-resolution spectrum of the BH Q-branch. This spectrum reveals the contribution of ^{11}B and ^{10}B. The label indicates the position of the ^{11}BH A-X (0,0) line connecting the rotational levels with the quantum numbers $J = J'$.

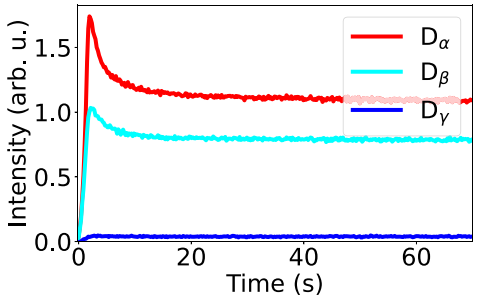

Fig. 6. Temporal evolution of the deuterium Balmer lines during discharges at the linear plasma device PSI-2. The line intensities reach a plateau phase after a few seconds, indicating a stable discharge.

estimation of erosion by measuring the layer thickness before and after plasma exposure, as presented in the following section. We performed the partial erosion experiments for floating potential (−43 V) to −100 V bias. Integrating across the emission of the B I 249.7 nm lines gives the data plotted in Fig. 8(a). In all cases, one observes the plateau of the emission for the first 70 s of the discharge. This plateau indicates that the boron layer still covers the complete surface of the tungsten target. In addition, the intensity of the atomic boron emission depends evidently on the kinetic energy of the bombarding ions. Increasing the ion impact energy intensifies the line emission of boron. This behavior matches the expectation since the physical sputtering yield has a strong gradient for near-threshold erosion [3].

The purple and blue curves plotted in Fig. 8 show the results from two long-pulse experiments. Firstly, we investigated a complete boron erosion experiment at a floating potential (−43 V). Here, the plateau of the emission survives for approximately 180 s, followed by the typical sharp drop once the surface is completely eroded. It is vital to note that the atomic emission signal detected is a measure of the gross erosion. Redeposition of the sputtered atoms can occur. In PSI-2, it depends on the ionization rates and momentum reversal that guides these particles back towards the target plate.

The most probable velocity of sputtered boron, according to Eq. (9) of [52], is on the order of 7 km s^{-1}, which is about three times faster than in the case of sputtered tungsten atoms. Estimating the ionization length (1/e value) based on the plasma parameters (T_e = 10 eV, n_e = 3×10^{17} m^{-3}) and the ionization rates tabulated in Table 2 of [53] yields a length of 0.8 m. The sputtering of the boron layers creates atoms with a wide range of velocities, as seen in the Thompson velocity distribution [54], including a fraction that moves at much lower speeds than the most probable velocity. These lower velocities drastically decrease the ionization length. Thus, a fraction of the sputtered boron can deposit on any surface in the chamber, such as on the target, Mo mask, W catcher samples, or steel walls. Once deposited, this boron can be re-eroded by particle bombardment, creating an influx of boron atoms into the plasma and contributing to the faint B I signal observed

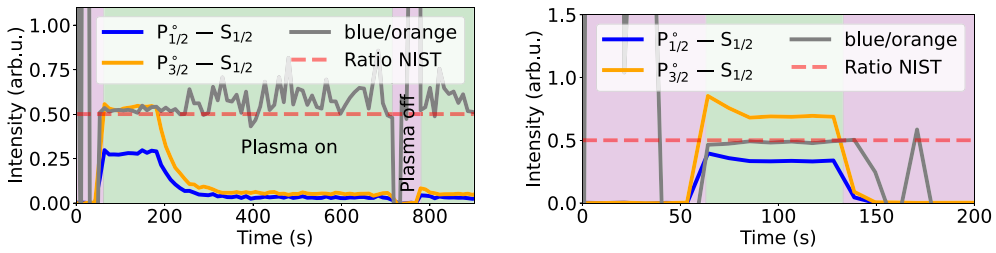

(a) Complete erosion −80 V bias, 26.11.2024 (b) Partial erosion −100 V bias, 25.11.2024

Fig. 7. Line emission by the 2p-3s doublet of boron during sputtering experiments at PSI-2. Areas shaded in green indicate the discharge was running, whereas the pink shaded area corresponds to the times without plasma operation. (a) shows a complete erosion experiment, where the line intensity drops quickly after the initial plateau phase of around 150 s. (b) presents the atomic emission during 70 s partial erosion experiment. The intensity does not exhibit the same decay behavior as in (a), indicating that the boron layer still covers the whole tungsten sample surface.

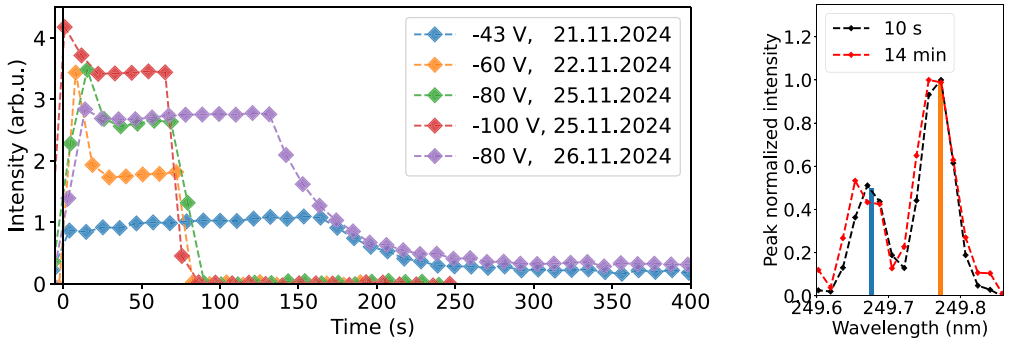

(a) B I 2p-3s emission intensity

(b) B I 2p-3s transitions during a long-pulse discharge

Fig. 8. (a) shows the time-resolved emission of the atomic boron 249.7 nm lines when varying the bias applied to the sample. The curves having a sharp cutoff after 70 s are due to partial erosion experiments. In that case, we terminated the discharge preemptively to maintain a complete boron layer on the sample. (b) shows that atomic boron line emission is present after 14 min (−80 V, repeated). This presence of atomic boron in the plasma might be due to redeposition on the sample holder.

after 20 min. Witness plates are foreseen for future experiments to study this contribution.

Finally, the erosion experiment at −80 V bias was repeated to verify the reproducibility of the experiments. Indeed, the atomic line emission agrees well with the previous short-pulse case (green, purple in Fig. 8(a)). The second goal was to check what happens to the B I emission after the erosion of the main boron layer when we only briefly turned off the plasma. The branching ratio method indicates that at the end of this discharge, at 14 min, boron is still measurable, as depicted in Fig. 8(b).

5.2. Molecular emission during erosion

Simultaneously, the emission by molecular BD was measured to monitor the chemical erosion at the surface. Note that the ionizing plasma conditions in these experiments are preventing the formation of BD in the plasma itself. The Littrow spectrometers measured the BD A-X (0,0) Q-branch emission, as presented in Figs. 9(a) to (d). The time resolution of the overview spectrometer was identical to that of the Czerny-Turner spectrometer (Section 5.2): 10 s. A 60 s integration time is required for the Echelle system to accumulate sufficient photons emitted by the BD molecule. This long integration time prevents time-resolved measurements during the 70 s pulsed discharges. However, the high-resolution measurements during the long-pulse experiments are vital for validating the modeling of the molecular band spectra and the temperature of the rotational level population.

The atomic line emission indicates that the boron layer still covers the whole tungsten sample for up to 150 s (Fig. 8(a)). Thus, the expectation is a strong molecular signal during this phase. To cover all significant contributions by BD, we summed up the first four minutes of the emission spectra, giving the blue-colored line in Fig. 9(a). The red-colored curve presents the sum of the spectra of the last four minutes. These overview spectra reveal that D_γ line emission is dominant. The gray-shaded area indicates the BD Q-branch. Subtracting the red data from the blue data points provides the black curve in Fig. 9(b), representing the sole contribution of the BD molecules. The fitting shows excellent agreement with the measured data. Figs. 9(c) and (d) present essentially the same but at a much higher spectral resolution. In particular, we see that other spectral lines pollute our BD Q-branch and that adequate interpretation of the data requires these long-term exposures to extract the contribution by the BD molecules. The rotational temperature derived from the high-resolution spectrum (T_{rot}=2829(73) K) differs by less than 3% from the overview spectrum (T_{rot}=2754(75) K). This minor difference is an excellent result, supporting the scheme of analysis.

Analyzing the individual spectra measured by the overview Littrow provides time-resolved information on the rotational temperature of BD. Fig. 10(a) presents the temperatures derived and compares them to the results from Figs. 9(b) and (d). The fitting indicates an essentially constant rotational temperature of 2800 K during the first 150 s. After this point, the temperature oscillates with a large amplitude, and the standard deviation of the fit becomes huge. Fig. 10(b) reveals the

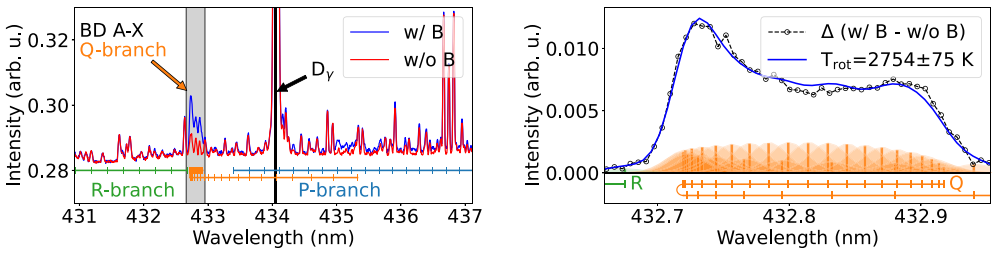

(a) Overview spectra with (w/) and without (w/o) B

(b) Difference (Δ) between the overview spectra with (w/) and without (w/o) B, as derived from Fig. 9 (a)

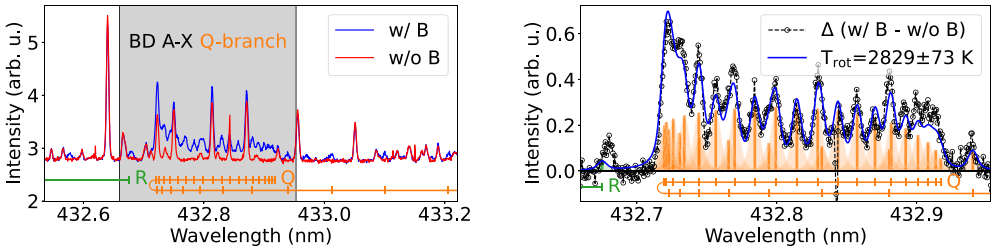

(c) High-resolution spectra with (w/) and without (w/o) B

(d) Difference (Δ) between the high-resolution spectra with (w/) and without (w/o) B, as derived from Fig. 9 (c)

Fig. 9. The spectra plotted as the blue lines in (a) and (c) correspond to cases where BD molecules are present. The red-colored lines are characteristic for cases without a significant amount of BD molecules. The areas shaded in gray for (a) and (c) indicate the position of the BD Q-branch. Subtracting the red from the blue spectra provides the spectroscopic finger print of the BD molecule. The fitting procedure captures for (b) and (d) the BD Q-branch and provides a rotational population temperature as an output. The color coding is consistent with Figs. 5(a) and (b).

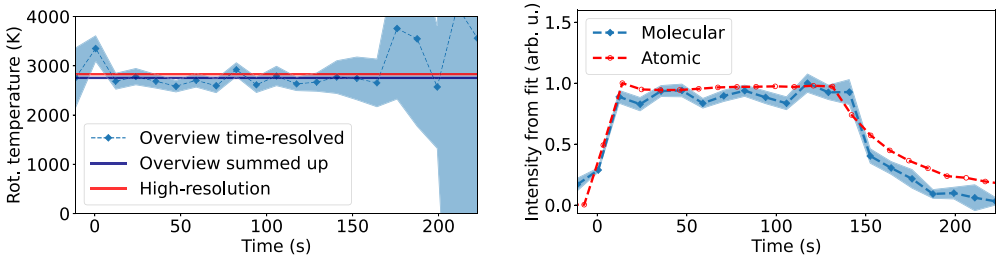

(a) Rotational temperature

(b) Time-resolved intensity of the molecular and atomic transitions

Fig. 10. (a) the rotational temperature as obtained from fitting the BD A-X (0,0) Q-branch. The shaded area indicates the standard deviation of the fit. (b) the time evolution of atomic and molecular emission is similar.

reason: This point in time merely corresponds to the case where the plasma eroded the original boron layer. Indeed, the atomic emission follows the same trend, showing the consistency of the atomic and molecular spectra.

6. Sputtering yield for boron

The 70 s pure deuterium discharges at PSI-2 lead to a partial erosion of the boron layer, leaving a homogeneous surface coverage of boron on tungsten. Afterward, the SEM(FIB) method provided the thickness of the boron layer, as described in Section 2.1. The difference in thickness before and after plasma exposure gives an estimate of the net erosion, and by normalizing to the exposure time, the erosion rates. Combining this with the ion flux densities and their kinetic energies from Figs. 2(a) and (b) makes it possible to derive the sputtering yields for boron by deuterons. Note that the erosion is inhomogeneous at the surface due to the peaked profile of the impinging deuterons and the impact energy. Thus, one measurement provides several erosion zones across the sample. Table 2 presents these sputtering yields.

Fig. 11 compares our sputtering yields to other experimental data [21] and BCA simulations [3]. The agreement with the data by Hechtl et al. [21] is very good. However, one has to keep the significant differences in the surface structure in mind: Hechtl et al. studied graphite substrates with plasma sprayed boron on top via mass loss. Both data sets exhibit a systematically higher sputtering yield than predicted by BCA. This difference might indicate that chemical erosion contributes noticeably.

The line intensity of the atomic boron emission also gives information on the physical sputtering yield. The approach to derive relative sputtering yields is identical to the procedure described in [55]. Appendix provides a brief explanation of the approximation.

Table 2
Sputtering yields derived from the post-mortem analysis via SEM(FIB), at the positions indicated in Fig. 2(b), after partial erosion experiments. Each bias voltage provides several erosion zones due to the radial gradient in plasma potential.

Position	2	1	3	2	1	2	1	2
Bias (V)	−43	−60	−43	−60	-80	−80	−100	−100
Energy (eV)	28.3	36.5	42.0	45.3	55.0	63.5	76.3	85.1
Yield	0.0064	0.011	0.01	0.012	0.015	0.015	0.024	0.03

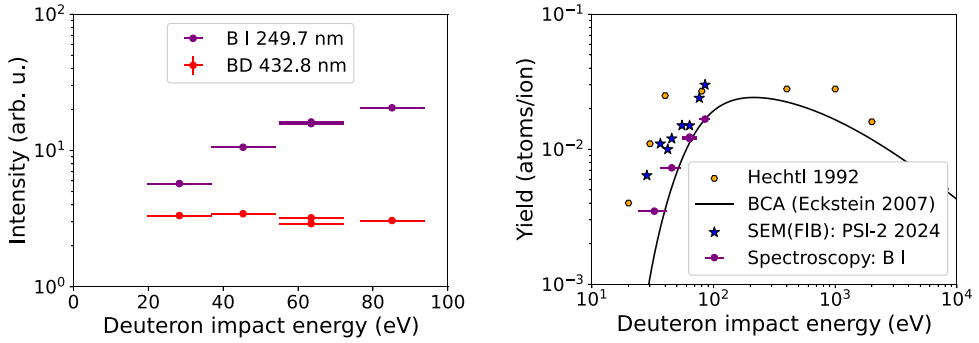

(a) Atomic and molecular emission (b) Sputtering yields

Fig. 11. (a) dependency of the atomic and molecular emission on the impact energy of the deuterons. (b) sputtering yields of boron by deuterium bombardment. The comparison to the atomic emission (Spectroscopy: B I) is on a relative scale only, as discussed in Appendix.

This approach gives the purple data points in Fig. 11(b). They agree well with the BCA approximation. Compared to that, the emission by the BD molecules stays essentially constant independent of the bias, as shown in Fig. 11(a). This behavior indicates a contribution of chemical erosion, whose absolute quantification by optical emission spectroscopy requires further investigation and knowledge of rate coefficients for electron impact excitation [56].

7. Conclusion

This work reported on plasma-boron layer interaction studies performed at the linear plasma device PSI-2. The goal was to investigate the erosion of a thin boron layer under low-energy deuteron bombardment, addressing the uncertainties on the sputtering yields. Boron layers of 115 nm thickness on tungsten substrates were produced via RF magnetron sputter deposition. Exposing these boron layers to deuterium discharges in the linear plasma device PSI-2 provided the bombardment with deuterons. In this case, the sample holder acquires a global floating potential of −43 V, providing the ions with the lowest possible kinetic energies (Section 2). Further biasing the target towards −100 V enabled a scan for the near-threshold erosion of the B layer by deuteron bombardment.

The time-resolved emission spectroscopy of the atomic boron and molecular BD provided information on the physical and chemical erosion, respectively. For this setup, the B I 2p-3s 249.7 nm transitions of boron represent a good choice of lines to monitor the atomic emission. In the case of BD, the rotational band spectra of the first excited transition, the standard BD A-X (0,0) Q-branch at 432.8 nm were recorded. Section 4 gave a detailed discussion on the transition selection and the rotational band modeling of the A-X transitions.

The molecular spectra recorded during deuterium plasma operation at PSI-2 (T_e=10 eV, n_e=3 × 10^{17} m^{-3}) suggest a constant rotational temperature of the BD molecules of 2800 K. Measuring overview spectra that also cover the D_γ line, and comparing them to high-resolution spectra that give information on individual lines of the BD A-X (0,0) Q-branch validated the rotational temperatures of the molecules. Thus, the consistent modeling of the BD emission gives high confidence in the analysis of the molecular spectroscopy.

The atomic and molecular signals behaved very similarly during long pulse experiments. Both exhibited a stable plateau-like emission phase during the first 150 s. The length of this plateau depends on the bias applied to the sample, so providing the deuterons with more energy shortened the plateau length from approximately 180 s to the above-mentioned 150 s. A rapid decay in line intensity follows this plateau, and the intensity stabilizes at a low level.

This continuous weak emission could hint at the migration of sputtered boron into zones with lower erosion rates. These long pulse experiments and erosion estimates using BCA gave high confidence that 70 s discharges should only partially erode the boron layers. Indeed, the atomic boron emission during the short pulses was terminated before the plateau phase of the emission ended. The thickness of the boron layer after plasma exposure gave information on the net erosion. Accounting for the exposure time, ion flux density, and plasma potential provided the sputtering yields as tabulated in Table 2. Additionally, the atomic and molecular spectroscopy gives complementary information on the gross erosion.

Fig. 11(b) shows these sputtering yields and indicates an excellent agreement with those from [21]. These yields are systematically higher than predicted from BCA. Nonetheless, the intensity of the B I emission, a measure of gross erosion, agrees reasonably well with the expectations from BCA. Contrary to that, the intensity of the molecular emission is practically independent of the bias applied to the sample. This behavior suggests a constant contribution of chemical erosion to the sputtering yields.

8. Outlook

Upcoming studies will focus on the line shape of the emission by atomic and molecular species. Evaluating the line shape by including all relevant broadening mechanisms (isotope shifts, hyperfine structure, Zeeman splitting, etc.) could provide additional information on the contributions of the physical and chemical erosion. For example, there might be two populations of atomic boron: energies in the eV range due to physical sputtering and energies sub eV due to dissociation of BD. So, in the case of boron, we will upgrade the high-resolution Littrow using UV optics. The tools developed for tungsten [41,55,57] will provide line-shape modeling. Future work will also extend the high-resolution studies of BD by a polarization scan to test the standard formulas of Zeeman splitting of molecules under our conditions [58,59].

CRediT authorship contribution statement

Marc Sackers: Writing – review & editing, Writing – original draft, Visualization, Validation, Software, Methodology, Investigation, Formal analysis, Data curation. **Oleksandr Marchuk:** Writing – review & editing, Validation, Supervision, Methodology, Investigation, Formal analysis, Data curation. **Anne Houben:** Writing – review & editing, Visualization, Validation, Supervision, Methodology, Investigation, Formal analysis, Data curation, Conceptualization. **Eduard Warkentin:** Writing – review & editing, Validation, Investigation, Formal analysis, Data curation. **Marcin Rasinski:** Writing – review & editing, Visualization, Validation, Methodology, Investigation, Formal analysis, Data curation. **Sebastijan Brezinsek:** Writing – review & editing, Validation, Supervision, Resources, Project administration, Funding acquisition, Data curation, Conceptualization. **Arkadi Kreter:** Writing – review & editing, Visualization, Validation, Resources, Formal analysis, Data curation, Conceptualization.

Declaration of competing interest

The authors declare that they have no known competing financial interests or personal relationships that could have appeared to influence the work reported in this paper.

Acknowledgments

This work has been carried out within the framework of the EUROfusion Consortium, funded by the European Union via the Euratom Research and Training Programme (Grant Agreement No 101052200 — EUROfusion). Views and opinions expressed are however those of the author(s) only and do not necessarily reflect those of the European Union or the European Commission. Neither the European Union nor the European Commission can be held responsible for them.

Appendix. Relative sputtering yields from spectroscopy

The average transport velocity of sputtered atoms is in a first-order approximation (Eq. (32) [55])

$$v_n = \frac{2}{3}\int v F_v(v)dv, \tag{A.1}$$

where F_v is the velocity distribution function. In this case, the Thompson particle flux density distribution (19) from [60], with the square root term, provides an estimate for the near-threshold erosion. The line intensity $I_{i\to j}$ of a transition from state i to j gives the sputtering yield, if the constant C and the average transport velocity are known as per Eq. (35) of [55]:

$$Y = \frac{I_{i\to j}}{C} v_n, \tag{A.2}$$

The emission detected at −100 V bias provides the constant as

$$C = \frac{I_{i\to j}}{Y_{BCA}(85.1\,eV)} v_n, \tag{A.3}$$

where $Y_{BCA}(85.1\,eV)$ is the BCA [3] sputtering yield at a kinetic energy of 85.1 eV, due to the difference between plasma potential and bias at position 2 of the target (cf. Fig. 2(b)). Using this constant in Eq. (A.2) provides the relative sputtering yields at the energies of 63.5 eV, 45.3 eV, and 28.3 eV.

Data availability

Data will be made available on request.

References

[1] R. Pitts, A. Loarte, T. Wauters, et al., Plasma-wall interaction impact of the ITER re-baseline, Nucl. Mater. Energy 42 (2025) 101854, http://dx.doi.org/10.1016/j.nme.2024.101854.
[2] A. Loarte, R.A. Pitts, T. Wauters, et al., The new ITER baseline, research plan and open R&D issues, Plasma Phys. Control. Fusion 67 (2025) 065023, http://dx.doi.org/10.1088/1361-6587/add9c9.
[3] R. Behrisch, W. Eckstein, Sputtering by Particle Bombardment: Experiments and Computer Calculations from Threshold to Mev Energies, vol. 110, Springer Science & Business Media, 2007.
[4] G. McCracken, P. Stott, Plasma-surface interactions in tokamaks, Nucl. Fusion 19 (7) (1979) 889, http://dx.doi.org/10.1088/0029-5515/19/7/004.
[5] J. Winter, H. Esser, L. Könen, et al., Boronization in textor, J. Nucl. Mater. 162–164 (1989) 713–723, http://dx.doi.org/10.1016/0022-3115(89)90352-8.
[6] U. Schneider, W. Poschenrieder, M. Bessenrodt-Weberpals, et al., Boronization of ASDEX, J. Nucl. Mater. 176–177 (1990) 350–356, http://dx.doi.org/10.1016/0022-3115(90)90071-T.
[7] J. Wu, J. Hu, Y. Chen, et al., Recent results of boronization on EAST and HT-7 superconducting tokamak, J. Nucl. Mater. 415 (1, Supplement) (2011) S1046–S1049, http://dx.doi.org/10.1016/j.jnucmat.2010.10.089.
[8] E. Wang, S. Brezinsek, S. Sereda, et al., Impurity sources and fluxes in W7-X: from the plasma-facing components to the edge layer, Phys. Scr. 2020 (T171) (2020) 014040, http://dx.doi.org/10.1088/1402-4896/ab4c04.
[9] J. Bucalossi, J. Achard, O. Agullo, et al., Operating a full tungsten actively cooled tokamak: overview of WEST first phase of operation, Nucl. Fusion 62 (4) (2022) 042007, http://dx.doi.org/10.1088/1741-4326/ac2525.
[10] V. Rohde, M. Balden, K. Krieger, R. Neu, Boronization with tungsten plasma-facing surfaces in ASDEX upgrade, Nucl. Mater. Energy 43 (2025) 101923, http://dx.doi.org/10.1016/j.nme.2025.101923.
[11] S. Ertmer, High-Resolution Spectroscopy Studies on Sputtered Atoms in the Linear Plasma Device PSI-2 (Ph.D. thesis), Ruhr-Universität Bochum, Universitätsbibliothek, 2022, http://dx.doi.org/10.13154/294-8580.
[12] J. Romazanov, D. Borodin, A. Kirschner, et al., First ERO2.0 modeling of be erosion and non-local transport in JET ITER-like wall, Phys. Scr. 2017 (T170) (2017) 014018, http://dx.doi.org/10.1088/1402-4896/aa89ca.
[13] J. Romazanov, S. Brezinsek, A. Kirschner, et al., First Monte-Carlo modelling of global beryllium migration in ITER using ERO2.0, Contrib. Plasma Phys. 60 (5–6) (2020) e201900149, http://dx.doi.org/10.1002/ctpp.201900149.
[14] J. Romazanov, S. Brezinsek, C. Baumann, et al., Validation of the ERO2.0 code using W7-X and JET experiments and predictions for ITER operation, Nucl. Fusion 64 (8) (2024) 086016, http://dx.doi.org/10.1088/1741-4326/ad5368.
[15] S. Rode, S. Brezinsek, A. Kirschner, et al., Multi-staged ERO2.0 simulation of material erosion and deposition in recessed ITER mirror assemblies, Nucl. Mater. Energy 38 (2024) 101564, http://dx.doi.org/10.1016/j.nme.2023.101564.
[16] S. Rode, S. Brezinsek, M. Groth, et al., Multi-staged ERO2.0 simulation of material erosion and deposition in recessed mirror assemblies in JET and ITER, Nucl. Fusion 64 (8) (2024) 086032, http://dx.doi.org/10.1088/1741-4326/ad556d.
[17] P. Mertens, The core-plasma CXRS diagnostic for ITER: an introduction to the current design, J. Fusion Energy 38 (3) (2019) 264–282, http://dx.doi.org/10.1007/s10894-018-0202-1.
[18] M. Amarika, G. Beaskoetxea, G. Murga, et al., ITER core plasma thomson scattering diagnostic design, Fusion Eng. Des. 203 (2024) 114416, http://dx.doi.org/10.1016/j.fusengdes.2024.114416.
[19] L. Dittrich, P. Petersson, H. Laabadi, et al., Impact of ion irradiation and film deposition on optical and fuel retention properties of Mo polycrystalline and single crystal mirrors, Nucl. Mater. Energy 37 (2023) 101548, http://dx.doi.org/10.1016/j.nme.2023.101548.
[20] K. Schmid, T. Wauters, Full W ITER: Assessment of expected W erosion and implications of boronization on fuel retention, Nucl. Mater. Energy 41 (2024) 101789, http://dx.doi.org/10.1016/j.nme.2024.101789.
[21] E. Hechtl, A. Mazanec, W. Eckstein, J. Roth, C. Garcia-Rosales, Sputtering behavior of boron and boron carbide, J. Nucl. Mater. 196–198 (1992) 713–716, http://dx.doi.org/10.1016/S0022-3115(06)80129-7.
[22] E. Vietzke, Energy distributions of CD4 and CD3 chemically released from graphite by D+ and D0/Ne+ impact, J. Nucl. Mater. 290–293 (2001) 158–161, http://dx.doi.org/10.1016/S0022-3115(00)00609-7.
[23] R.K. Janev, D. Reiter, U. Samm, Collision Processes in Low-Temperature Hydrogen Plasmas, vol. 4105, Forschungszentrum, Zentralbibliothek Jülich, 2003.
[24] R.K. Janev, D. Reiter, Collision processes of CHy and CHy+ hydrocarbons with plasma electrons and protons, Phys. Plasmas 9 (9) (2002) 4071–4081, http://dx.doi.org/10.1063/1.1500735.
[25] A. Kreter, C. Brandt, A. Huber, et al., Linear plasma device PSI-2 for plasma-material interaction studies, Fusion Sci. Technol. 68 (1) (2015) 8–14, http://dx.doi.org/10.13182/FST14-906.
[26] I. Sorokin, I. Vizgalov, V. Kurnaev, et al., In-situ mass-spectrometer of magnetized plasmas, Nucl. Mater. Energy 12 (2017) 1243–1247, http://dx.doi.org/10.1016/j.nme.2017.01.015.

[27] J. Schmitz, Development of Tungsten Alloy Plasma-Facing Materials for the Fusion Power Plant (Ph.D. thesis), Universiteit Gent. Faculteit Ingenieurswetenschappen en Architectuur ; Ruhr-Universität Bochum. Faculty of Physics and Astronomy, Ghent University, 2020, p. xv, 176.
[28] A. Houben, E. Warkentin, M. Rasinski, et al., Boron layer preparation, characterization and hydrogen isotope permeability for fusion application, Submitt. Nucl. Mater. Energy (2025).
[29] M. Rasiński, S. Brezinsek, A. Kreter, et al., FIB line marking as a tool for local erosion/deposition/fuzz formation measurements in ASDEX upgrade during the he campaign, Nucl. Mater. Energy 37 (2023) 101539, http://dx.doi.org/10.1016/j.nme.2023.101539.
[30] N. Matsunami, Y. Yamamura, Y. Itikawa, et al., Energy dependence of the ion-induced sputtering yields of monatomic solids, At. Data Nucl. Data Tables 31 (1) (1984) 1–80, http://dx.doi.org/10.1016/0092-640X(84)90016-0.
[31] H.-J. Kunze, Introduction to Plasma Spectroscopy, vol. 56, Springer Science & Business Media, 2009.
[32] M. Born, E. Wolf, Principles of Optics: Electromagnetic Theory of Propagation, Interference and Diffraction of Light, Elsevier, 2013.
[33] G.K. Woodgate, Elementary Atomic Structure, Oxford University Press, 1983.
[34] A. Kramida, Y. Ralchenko, J. Reader, NIST ASD Team, NIST Atomic Spectra Database, NIST Standard Reference Database 78 (Version 5.12), National Institute of Standards and Technology, 2024, http://dx.doi.org/10.18434/T4W30F.
[35] H.P. Summers, The ADAS user manual, version 2.6., 2004, URL http://www.adas.ac.uk/.
[36] P. Jönsson, C. Froese Fischer, Large-scale multiconfiguration hartree-fock and configuration-interaction calculations of isotope shifts and hyperfine structures in boron, Phys. Rev. A 50 (1994) 3080–3088, http://dx.doi.org/10.1103/PhysRevA.50.3080.
[37] B. Maaß, T. Hüther, K. König, et al., Nuclear charge radii of ^{10,11}B, Phys. Rev. Lett. 122 (2019) 182501, http://dx.doi.org/10.1103/PhysRevLett.122.182501.
[38] B. Maaß, Laser Spectroscopy of the Boron Isotopic Chain (Ph.D. thesis), Technische University Darmstadt (Germany). Fachbereich Physik, 2020.
[39] B. Lomanowski, Visible and Near-Infrared Divertor Spectroscopy on the MAST and JET-ILW Tokamaks (Ph.D. thesis), Durham University, 2015.
[40] S.M. Sze, Y. Li, K.K. Ng, Physics of Semiconductor Devices, John wiley & sons, 2021.
[41] M. Sackers, O. Marchuk, S. Ertmer, et al., High-resolution emission spectroscopy of w I lines: Comparing near-threshold sputtering of mono- and polycrystalline tungsten by Ar ions, Phys. Plasmas 31 (12) (2024) 123505, http://dx.doi.org/10.1063/5.0233271.
[42] E. Miliordos, A. Mavridis, Ab initio investigation of the electronic structure and bonding of BH, BH-, and HBBH molecules, J. Chem. Phys. 128 (14) (2008) 144308, http://dx.doi.org/10.1063/1.2902284.
[43] S. Brezinsek, R. Pugno, U. Fantz, et al., Determination of photon efficiencies and hydrocarbon influxes in the detached outer divertor plasma of ASDEX upgrade, Phys. Scr. 2007 (T128) (2007) 40, http://dx.doi.org/10.1088/0031-8949/2007/T128/008.
[44] B. Karthikeyan, S. Bagare, N. Rajamanickam, V. Raja, On the search for BF, BH and BS molecular lines in sunspot spectra, Astropart. Phys. 31 (1) (2009) 6–12, http://dx.doi.org/10.1016/j.astropartphys.2008.10.009.
[45] R.J. Hendricks, D.A. Holland, S. Truppe, et al., Vibrational branching ratios and hyperfine structure of 11BH and its suitability for laser cooling, Front. Phys. Volume 2 - 2014 (2014) 51, http://dx.doi.org/10.3389/fphy.2014.00051.
[46] T. Kawate, N. Ashikawa, M. Goto, et al., Experimental study on boron distribution and transport at plasma-facing components during impurity powder dropping in the large helical device, Nucl. Fusion 62 (12) (2022) 126052, http://dx.doi.org/10.1088/1741-4326/ac9ac6.
[47] S. Mahmood, N.M. Shaikh, M. Kalyar, et al., Measurements of electron density, temperature and photoionization cross sections of the excited states of neon in a discharge plasma, J. Quant. Spectrosc. Radiat. Transfer 110 (17) (2009) 1840–1850, http://dx.doi.org/10.1016/j.jqsrt.2009.03.029.
[48] W. Fernando, P. Bernath, Fourier transform spectroscopy of the A1Π -X1Σ + transition of BH and BD, J. Mol. Spectrosc. 145 (2) (1991) 392–402, http://dx.doi.org/10.1016/0022-2852(91)90126-U.
[49] W.-T. Luh, W.C. Stwalley, The X1Σ+, A1Π, and B1Σ+ potential energy curves and spectroscopy of BH, J. Mol. Spectrosc. 102 (1) (1983) 212–223, http://dx.doi.org/10.1016/0022-2852(83)90239-4.
[50] G. Herzberg, Molecular Spectra and Molecular Structure. Vol. 1: Spectra of Diatomic Molecules, Van Nostrand Reinhold, New York, 1950.
[51] C.M. Western, PGOPHER: A program for simulating rotational, vibrational and electronic spectra, J. Quant. Spectrosc. Radiat. Transfer 186 (2017) 221–242, http://dx.doi.org/10.1016/j.jqsrt.2016.04.010.
[52] M. Sackers, O. Marchuk, S. Ertmer, S. Brezinsek, A. Kreter, Space-resolved line shape model for sputtered atoms of finite-size targets, Phys. Scr. 98 (11) (2023) 115603, http://dx.doi.org/10.1088/1402-4896/acfe4a.
[53] G. Voronov, A practical fit formula for ionization rate coefficients of atoms and ions by electron impact:Z=1–28, At. Data Nucl. Data Tables 65 (1) (1997) 1–35, http://dx.doi.org/10.1006/adnd.1997.0732.
[54] M. Thompson, The velocity distribution of sputtered atoms, Nucl. Instrum. Methods Phys. Res. Sect. B: Beam Interact. Mater. Atoms 18 (1) (1986) 411–429, http://dx.doi.org/10.1016/S0168-583X(86)80067-2.
[55] M. Sackers, C. Busch, T.V. Tsankov, et al., Plasma parameters and tungsten sputter rates in a high-frequency CCP, Phys. Plasmas 29 (4) (2022) 043511, http://dx.doi.org/10.1063/5.0083613.
[56] T. Kawate, I. Murakami, M. Goto, Calculation of electronic excitation cross sections and rate coefficients for boron monohydride (BH), Plasma Sources Sci. Technol. 32 (8) (2023) 085006, http://dx.doi.org/10.1088/1361-6595/acec0c.
[57] M. Sackers, O. Marchuk, D. Dipti, et al., Zeeman effect of isotopes of Kr and Xe investigated at the linear plasma device PSI-2, Plasma Sources Sci. Technol. 33 (2) (2024) 025015, http://dx.doi.org/10.1088/1361-6595/ad23fa.
[58] E.C. Kemble, R.S. Mulliken, F.H. Crawford, The zeeman effect in the angstrom CO bands, Phys. Rev. 30 (1927) 438–457, http://dx.doi.org/10.1103/PhysRev.30.438.
[59] F.H. Crawford, Zeeman effect in diatomic molecular spectra, Rev. Modern Phys. 6 (1934) 90–117, http://dx.doi.org/10.1103/RevModPhys.6.90.
[60] M.W. Thompson, II. The energy spectrum of ejected atoms during the high energy sputtering of gold, Philos. Mag.: A J. Theor. Exp. Appl. Phys. 18 (152) (1968) 377–414, http://dx.doi.org/10.1080/14786436808227358.